Resonant Rotational Reluctance Actuator for Large Range Scanning Mirrors

Daniel Pechgraber, Ernst Csencsics and Georg Schitter, *Senior Member, IEEE*

***Abstract*—This paper presents the design, manufacturing and evaluation of a scanning mirror system based on a novel resonant rotational reluctance actuator. The system comprises a ferromagnetic mover with a 15mm aperture, which is actuated by the reluctance force generated by an actuator coil, whose magnetic flux is guided via a ferromagnetic yoke. An integrated angular position sensor system based on optical proximity sensors enables feedback control of the scanning amplitude. The actuator design locates the ferromagnetic yoke on the side of the mover, allowing for a large scanning range of ± 13.5deg mechanical with a scanning frequency of 223Hz. This outperforms the state-of-the-art systems in the performance metric scanning range times aperture size.**

***Index Terms*—Scanning mirror system, reluctance actuator, large range, large aperture.**

I. Introduction

SCANNING mirror systems are devices, which reflect an incoming light beam and change its direction in a proper way. They are used in various different applications including systems for confocal microscopy [1], scanning optical lithography [2], optical coherence topography [3], light detection and ranging (LiDAR)[4], SLA 3D-printing [5], and micro-machining [6].

Scanning mirrors can be categorized in non-resonant and resonant systems. Non-resonant systems are capable of pointing the mirror in one static direction and to perform arbitrary motion patterns [7]. Resonant scanning mirrors by contrast are driven at the resonance frequency of their mechanical structure, in order to reach high scanning amplitudes [8]. The scanning range of the system increases the optical field of view (FoV) of the reflected laser beam. Therefore the product of scanning range times mirror aperture size in combination with the scanning frequency is an important performance metric for these systems [8], [9].

The reflecting mirror aperture is usually only in the order of single millimeters for very fast systems with a scanning frequency of greater $2\,\mathrm{kHz}$ [10], [11]. However, for some applications larger aperture sizes are desirable, because of the required waist of the reflected laser beam, such as SLA 3D-printing [12] or micro-machining [6]. Beam diameters of $6\,\mathrm{mm}$ and more are commonly used in these applications [6].

For larger reflecting mirrors usually macroscopic fast steering mirror (FSM) systems are used, which are commonly actuated by Lorentz-force based voice-coil actuators for larger scan range or piezo-electric actuators for higher bandwidth [13]. Lorentz-force based systems with aperture sizes of $5.5\,\mathrm{mm}$ and $8\,\mathrm{mm}$ achieve mechanical scanning ranges of $\pm 15.5\,\mathrm{deg}$ and $\pm 22.5\,\mathrm{deg}$ at their resonance frequencies of $192\,\mathrm{Hz}$ [14] and $60\,\mathrm{Hz}$ [15] respectively. The latter system represents the best performing system in the metric scanning range times mirror aperture size with $180\mathrm{deg} \cdot \mathrm{mm}$. Reluctance force, although not frequently used yet, is reported to relax the trade-off between scanning range and bandwidth by a larger force constant as compared to Lorentz-force based systems [16]. In a hybrid reluctance force based two degree of freedom (2DoF) non-resonant tip/tilt system with a large mover aperture of $56\,\mathrm{mm}$, a mechanical scanning range of $\pm 3\,\mathrm{deg}$ and a closed-loop system bandwidth of $1\,\mathrm{kHz}$ is achieved [13]. The larger force constant is also beneficial for resonant systems, because the system efficiency can be further increased. A resonant reluctance actuated system is proposed in [17], in which a ferromagnetic nickel film is electroplated onto a silicon wafer, that is used as flexure and reflecting mirror. When driven at its resonance frequency of $1870\,\mathrm{Hz}$ a scanning range of $\pm 7.6\,\mathrm{deg}$ is achieved, but with the drawback of a small mirror aperture of $6.5\,\mathrm{mm}$.

The proposed reluctance actuated systems have in common, that the driving coils are located beneath the mover and therefore the motion range is restricted by the air gap to the mover. This requires a trade-off between achievable reluctance force, which is higher for smaller air-gaps, and achievable scanning range [16].

The main contribution of this paper is the design of a novel resonant rotational reluctance actuator integrated into a 1 DoF scanning mirror system with large aperture, which removes the mechanical restriction of currently proposed reluctance actuators by placing the ferromagnetic yoke on the side of the mover. Additionally a control strategy is developed, for stabilizing the scanning amplitude at arbitrary values.

In Section II the performance goals for the designed scanning mirror system are formulated and the working principle of the resonant rotational reluctance actuator is discussed. Further the detailed magnetical and mechanical system design are covered. Section III introduces the manufactured system prototype and presents the control strategy. The experimental results are shown in Section IV, which lead to the conclusion of the paper in Section V.

II. System Description

To meet the requirements on the mirror aperture size for applications which utilize large size laser beams of e.g. $10\,\mathrm{mm}$, a mover size of at least $15\,\mathrm{mm}$ is desired for the designed

Manuscript received Month 2xxx; revised Month xx, 2xxx; accepted Month xx, 2xxxx. Automation and Control Institute (ACIN), Technsiche Universität Wien, 1040 Vienna. Corresponding author: pechgraber@acin.tuwien.ac.at

Post-print version of the article: D. Pechgraber, E. Csencsics, and G. Schitter, “Resonant Rotational Reluctance Actuator for Large Range Scanning Mirrors,” *IEEE/ASME Transactions on Mechatronics*, 2023. DOI: 10.1109/TMECH.2023.3252940

TABLE I
PERFORMANCE GOALS OF THE SCANNING MIRROR SYSTEM

Parameter	Desired performance
Mirror aperture	15 mm
Scanning range	±12 deg
Scanning frequency	200 Hz

system. This takes into account that the effective footprint of the laser beam on the mirror is bigger than the laser spot diameter by the factor $1/\cos(\alpha)$, if α denotes the incident angle of the laser beam. The total optical FoV of laser scanners in this application field is in the range of 45 deg [18]. Therefore a mechanical scanning range of at least ±12 deg is desired (48 deg optical FoV). The scanning frequency should be as high as possible. However, the target is set to 200 Hz, which in combination with the other performance goals represents the state-of-the-art by means of an adopted performance metric for non-resonant 2DoF laser scanners presented in [9]. This performance metric is calculated as $\theta\sqrt{4A/\pi}f$, where θ, A and f are the total optical FoV, the mirror area and the resonant frequency, respectively. The targeted performance goals for the scanning system are summarized in Table I.

A. Actuator Working Principle

In Fig. 1 the working principle of the proposed resonant rotational reluctance actuator is depicted. It mainly relies on a ferromagnetic mover, that is suspended by a flexure structure in a way, that it can rotate around its rotation axis (parallel to x-axis) and is restricted in its other DoF. For generating the desired scanning motion, the mover is actuated in this rotational DoF by the reluctance force between the ends of a ferromagnetic yoke and the mover. In the presence of a magnetic flux (green dashed lines), the reluctance force $\vec{F}_r$ acts on the mover. If the mover is deflected from its equilibrium position ($\theta = 0$) with the angle $|\theta| > 0$, the force components perpendicular to the mover $F_r^{\perp}$ result in a net torque around the rotational axis directed back to the equilibrium position. This torque can be approximated by

$$\tau = 2F_r^{\perp}\frac{D}{2} = F_r^{\perp}D \tag{1}$$

with D denoting the length of the mover.

The reluctance force is proportional to the square of the coil current i_{act}, and thus a solely attractive force [19]. Hence, only pulling forces can be applied to the mover in this configuration. However, the same holds true for resonant MEMS mirrors driven with electro-static comb-drives, whose actuation principle also relies only on pulling forces [20]. These systems are usually driven by a square-wave signal with twice the oscillating frequency of the mover, which is called first-order parametric resonance [21]. Operation of the system is then possible at the vicinity of its resonance frequency, but not at arbitrary frequencies as in classical direct force excitation. In a similar manner this principle is applied to the proposed actuator. The actuator coil current is driven with the frequency f_a synchronized to the mover frequency f_m, in order to drive the mover in first-order parametric resonance ($f_a = 2f_m$). In

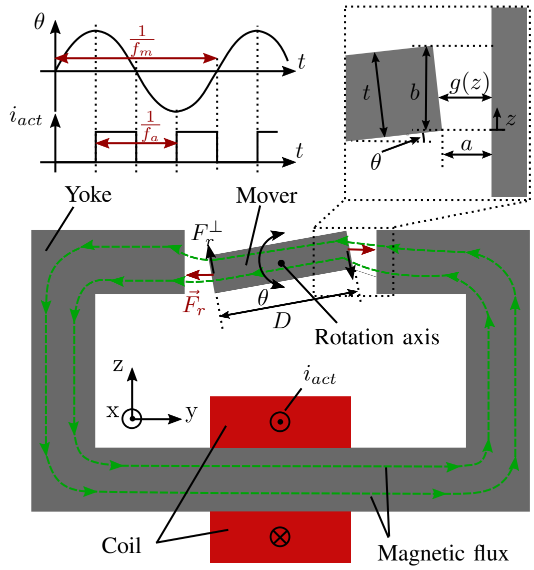

Fig. 1. Working principle of the proposed resonant rotational reluctance actuator: The magnetic flux generated by the current in the actuator coil i_{act} is guided to the mover via a ferromagnetic yoke. The current is controlled in a way, that the reluctance force upholds an oscillating motion of the mover around its rotation axis.

Fig. 1 the ideal case is shown, in which the current is switched on exactly at the peak of the mover oscillation and switched off in the equilibrium position, avoiding a pulling back of the mover.

A consequence of the operation in first-order parametric resonance is the destabilization of the movers equilibrium position at $\theta = 0$ [22]. For this reason, already small perturbations from the equilibrium position, like vibrations or mounting tolerances lead to the start of the mover oscillation. Therefore, the automatic startup of the system is possible by simply applying the mentioned actuation signal to the actuator.

B. Reluctance Torque on Mover

In order to estimate the reluctance torque on the mover for varying inclination angles θ and actuator coil currents i_{act} a simplified analytical model is derived based on the approach presented in [23]. The asymmetric air gap between the mover and the yoke, as can be seen in Fig. 1, is modeled as magnetic circuit consisting of a set of infinite reluctances in parallel. The corresponding air gap length along the mover edge is given by

$$g(z) = a + z\tan(\theta) \tag{2}$$

with a denoting the minimum distance from the mover to the yoke for a given mover angle θ, and b denoting the mover height along the z-axis. With the mover width T the differential permeance along the z-axis is then given by [23]

$$\mathrm{d}P(z) = \frac{\mu_0 T}{a + z\tan(\theta)}\,. \tag{3}$$

Evaluation of the integral $P = \int_0^b \mathrm{d}P(z)\,\mathrm{d}z$ yields the reluctance of one air gap $R_g = 1/P$ and the total reluctance

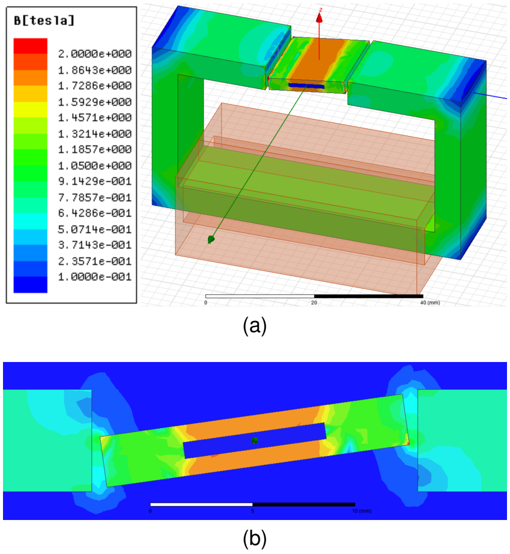

Fig. 2. Magnetostatic FEM analysis. (a) 3D FEM model of the actuator (b) Distribution of the magnetic flux density with $\theta = 8\,\mathrm{deg}$ and $i_{act} = 3\,\mathrm{A}$.

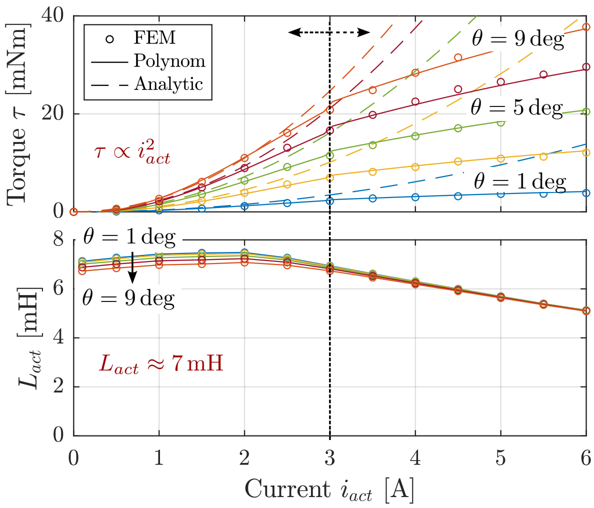

Fig. 3. Results of magnetostatic FEM analysis compared to the derived analytical model for the reluctance torque on the mover. In the region before saturation ($i_{act} < 3\,\mathrm{A}$) the torque on the mover τ is approximately proportional to i_{act}^2. The inductance L_{act} is $\approx 7\,\mathrm{mH}$ in this region.

of the whole magnetic circuit $R_t = 2R_g$ if the reluctance of the ferromagnetic yoke is neglected.

The reluctance force generated by the flux $\Phi = BA$ through a section A is given by [23]

$$F_r = \frac{\phi^2}{2\mu_0 A} \,. \tag{4}$$

As the air gap is modelled by a set of infinite parallel paths, the flux can be defined as

$$\mathrm{d}\phi(z) = N i_{act} \frac{R_g}{R_t} \,\mathrm{d}P(z) = \frac{N i_{act}}{2} \,\mathrm{d}P(z) \,, \tag{5}$$

and hence the reluctance force as

$$\mathrm{d}F_r(z) = \frac{\mathrm{d}\phi^2(z)}{2\mu_0 T \,\mathrm{d}z} \,. \tag{6}$$

Evaluation of the integral $\int_0^b \mathrm{d}F_r(z)\,\mathrm{d}z$ and geometrical considerations lead to the reluctance force of one air gap

$$F_r = \frac{N^2 i_{act}^2 \mu_0 T b}{8a\,(\tan(\theta)\, b + a)} \tag{7}$$

and

$$a(\theta) = g_{nom} - \frac{d}{2}\sin(\theta) + \frac{D}{2}\sin(\theta)\tan\left(\frac{\theta}{2}\right) \tag{8}$$

for the distance a and the nominal air gap length g_{nom} for $\theta = 0\,\mathrm{deg}$. By using (1), $F_r^{\perp} = F_r \sin(\theta)$ and $b(\theta) = t\cos(\theta)$ an analytic expression for the reluctance torque on the mover is given by

$$\tau(i_{act}, \theta) = \frac{D N^2 i_{act}^2 \mu_0 T b(\theta)}{8a(\theta)\,(\tan(\theta)\, b(\theta) + a(\theta))} \sin(\theta) \,. \tag{9}$$

C. Magnetostatic FEM Analysis

To verfiy the derived analytical model and to get more insights into the magnetic field distribution in the actuator, the system is analysed using ANSYS Maxwell (ANSYS Inc., Canonsburg, PA, USA). Figure 2a shows the 3D FEM model of the actuator, consisting of the actuator coil, the yoke and the mover with an air gap, accounting for the mount of the required suspension strucuture. The coil generates a magnetomotive force $\Theta = N i_{act}$ dependent on the applied current i_{act} and the number of windings N ($N = 250$ is assumed in the simulation). The mover size is 15x15x2.5 mm, complying with the performance goals from Table I, and the yoke is 60 mm wide, 35 mm high and 5 mm thick.

In Fig. 2b the distribution of the magnetic flux density is shown, when the mover is deflected from its equilibrium point ($\theta = 8\,\mathrm{deg}$) and a current of $i_{act} = 3\,\mathrm{A}$ is applied to the actuator coil. The reluctance force generated by the magnetic flux results in a torque that is directed back to the equilibrium position. Further, it can be seen, that the flux density is higher in the center of the mover, because the non-ferromagnetic suspension structure reduces the cross-section for the magnetic flux.

The dependency of the reluctance torque τ and the actuator inductance L_{act} on the coil current i_{act} and the mover angle θ is shown in Fig. 3. Due to the symmetry around the equilibrium position the mechanical angle is only varied in one direction. At lower currents the torque is approximately proportional to i_{act}^2, which is also confirmed by the analytical model (9). In the range of $i_{act} \approx 3\,\mathrm{A}$ saturation effects in the mover arise, which more and more lead to a deviation from the quadratic relation. Up to that point, the FEM analysis matches the derived analytical model well, confirming the validity of expression (9) as a design guideline for this type of actuator, at least in the range before the non-modelled saturation effects

Post-print version of the article: D. Pechgraber, E. Csencsics, and G. Schitter, "Resonant Rotational Reluctance Actuator for Large Range Scanning Mirrors," *IEEE/ASME Transactions on Mechatronics*, 2023. DOI: 10.1109/TMECH.2023.3252940

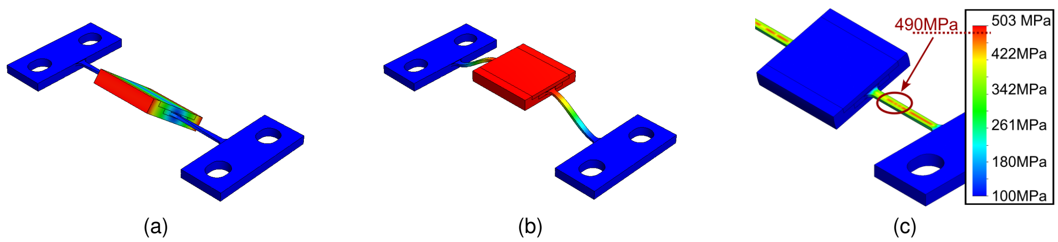

Fig. 4. Mechanical FEM analysis of aluminium flexure (a) The desired rotational mode at 241 Hz. (b) Piston mode at 259 Hz. (c) Mechanical stress distribution in the torsional beam flexure at a mover angle $\theta = 14$ deg. The stress limit in the material is almost reached (Tensile strength: 503 MPa).

TABLE II
COEFFICIENTS OF POLYNOMIAL APPROXIMATION

Coefficient	$i_{act} \leq 3$ A	$i_{act} > 3$ A	Unit
p_1	−0.1589	0.9530	$\mathrm{mN\,m/(deg \cdot A)}$
p_2	0.5385	−0.0411	$\mathrm{mN\,m/(deg \cdot A^2)}$
p_3	−0.0749	−0.00038	$\mathrm{mN\,m/(deg \cdot A^3)}$

occur. Over the entire simulated range an approximately linear relation with respect to θ can be observed. To gather an analytic expression for the reluctance torque based on the FEM analysis over the entire range, the simulated curves are split at $i_{act} = 3$ A and for either part a two dimensional polynomial function is fitted [24]:

$$\tau_{fit}(i_{act}, \theta) = p_1 \theta i_{act} + p_2 \theta i_{act}^2 + p_3 \theta i_{act}^3 \,, \tag{10}$$

with p_1, p_2 and p_3 being the polynomial coefficients delivers the best fit for the simulated data. This polynomial structure also ensures, that the boundary conditions

$$\tau_{fit} = 0 \quad \text{for} \quad \theta = 0\,\text{deg}\,, \quad \text{and} \tag{11a}$$

$$\tau_{fit} = 0 \quad \text{for} \quad i_{act} = 0\,\text{A} \tag{11b}$$

are fulfilled.

The polynomial coefficients are summarized in Table II. As can be seen, p_2 is the dominant coefficient for $i_{act} < 3$ A, again confirming the quadratic relation between the torque and the current.

The inductance of the actuator L_{act} is defined by

$$L_{act} = \frac{\Psi}{i_{act}} = \frac{N\Phi}{i_{act}} \tag{12}$$

with the flux linkage in the inductor $\Psi = N\Phi$. Similar to the torque curve, the saturation effects, reducing the effective inductance, can be seen at $i_{act} > 3$ A. Until this point, the inductance is approximately constant with $L_{act} = 7$ mH. Further, it is visible that the inductance only shows an insignificant dependency on the mover angle θ.

D. Mechanical System Design

To integrate the resonant rotational reluctance actuator into a scanning mirror system with the desired performance from Table I, a proper suspension structure is required. From an integrated system design's perspective there exist different design goals that can be summarized as follows:

1) Provide a suspension structure for the mover, which separates the eigenfrequency of the desired rotational mode from internal mode shapes, in order to minimize deviations from the ideal motion of the mover.
2) Minimize the moment of inertia of the mover for a given aperture size and suspension structure, in order to maximize the frequency of the desired rotational mode.
3) Minimize the magnetic resistance of the yoke and the mover in order to guide the magnetic flux due to the reluctance actuation principle.

The first goal is met by the use of a torsional beam flexure structure, which is already successfully used in another large aperture scanning mirror system with comparable dimensions [25]. Its torsional stiffness k_t, which determines the eigenfrequency of the rotational DoF together with the mover inertia J, is given by [26]

$$k_t = \frac{Gwh^3}{8l}\left(5.33 - 3.36\frac{h}{w}\left(1 - \frac{h^4}{12w^4}\right)\right)\,, \tag{13}$$

with w, h and l being the width, height and length of the torsional beam respectively, and G the shear modulus of the used material. In addition to (13), analytical formulas for the eigenfrequency calculation of the first 5 mode shapes of torsional beam flexures in combination with a mover are available in [26]. With these formulas and the geometric degrees of freedom (w, h, l and mover thickness t), the torsional stiffness can be tuned, by also realizing good frequency separation from the other eigenmodes.

However, to exploit the advantages of the proposed location of the yokes on the side of the mover and reaching the targeted scanning range, the mechanical stress capability of the used flexure material also has to be considered. The shear stress applied on a torsional beam can be calculated by [27]

$$\tau_{shear} = \frac{\beta G w}{2\alpha l}\theta_{max} \leq \tau_{max}\,, \tag{14}$$

where α and β are coefficients related to the width w and height h of the flexure, G is again the shear modulus and τ_{max} is the shear strength of the material [28]. The analytic formulas for the eigenfrequency tuning and (14) lead to contradicting requirements for some geometrical parameters of the flexure or the mover. Therefore an additional trade-off has to be made to keep the shear stress in the admissible range.

For the given aperture size, the second goal can be achieved by the use of a lighter material or by making the mover

Post-print version of the article: D. Pechgraber, E. Csencsics, and G. Schitter, "Resonant Rotational Reluctance Actuator for Large Range Scanning Mirrors," *IEEE/ASME Transactions on Mechatronics*, 2023. DOI: 10.1109/TMECH.2023.3252940

thinner. This goal partly conflicts with the third goal to minimize the magnetic resistance of the mover and the yoke. A ferromagnetic steel (S235JR) is used for the fabrication of these parts, in order to achieve this low magnetic resistance. However, the used ferromagnetic steel has a saturation flux density of $B \approx 1.9\,\mathrm{T}$, which leads to an increase of the magnetic resistance of the mover [29]. Therefore a reduction of the mover thickness, which corresponds to reducing the cross-section for the magnetic flux, limits the attainable flux density in the air gap and hence the reluctance force on the mover. As a trade-off a mover thickness of $2.5\,\mathrm{mm}$ is chosen, using results from the magnetostatic FEM analysis from the previous section. The air-gap, between the mover and the yoke is chosen to be $0.5\,\mathrm{mm}$, to avoid collisions of the mover with the yoke during oscillation due to mounting tolerances.

In Table III the final geometric properties of the torsional beam flexure and mover combination are summarized. A modal FEM analysis carried out in SolidWorks (Dassault Systèmes, Vélizy-Villacoublay, France) revealed an eigenfrequency of $241\,\mathrm{Hz}$ for the desired rotational mode and a frequency of $259\,\mathrm{Hz}$ for the unwanted piston mode, which is a result of making the flexure longer for reducing the shear stress. By increasing the flexure height and decreasing the width, the piston mode frequency can be shifted up, but at the same time the in-plane mode shape in y-direction would fall into the range of the rotational mode. Additionally the higher stiffness in y-direction reduces the influence of offset forces on the mover in y-direction due to slightly different air-gaps resulting from mounting tolerances. The resulting mode shapes are shown in Fig. 4a and Fig. 4b. Further modes occur at $645\,\mathrm{Hz}$, $849\,\mathrm{Hz}$ and $1491\,\mathrm{Hz}$ and are not expected to be excited, due to their mode shape and frequency separation to the rotational mode. In Fig. 4c, the result of a mechanical stress analysis for the used flexure material (Aluminium EN AW-7075) is shown. The results indicate, that the maximum scanning angle not exceeding the materials stress capability is in the range of $\pm 14\,\mathrm{deg}$ mechanical, which complies with the target range. It is to note, that for long-term operation under periodical stress this maximum scanning angle has to be reduced accordingly due to fatigue of the flexure material.

In Fig. 5 the details of the scanning mirror system with the integrated resonant rotational reluctance actuator are shown. The mover is connected to a supporting frame via the torsional beam flexure. The supporting frame is designed with much higher stiffness than the flexure, with the first eigenmode occuring at $\approx 10\,\mathrm{kHz}$, not affecting the rotational motion of the mover. The ferromagnetic yoke and the actuator coil are also connected to the frame via mounting brackets. A damping screw is located beneath the mover, to prevent the excitation of the unwanted piston mode from Fig. 4b. The screw has a sharpened tip and touches the mover from the bottom, in order not to obstruct the rotational motion, similar to the design in [13]. To enable feedback control of the scanning amplitude an angular position sensor system is required, which can also be seen beneath the mover.

TABLE III
GEOMETRICAL PROPERTIES

Parameter	Value
Mover thickness t	$2.5\,\mathrm{mm}$
Beam width w	$1.2\,\mathrm{mm}$
Beam height h	$0.5\,\mathrm{mm}$
Beam length l	$13\,\mathrm{mm}$

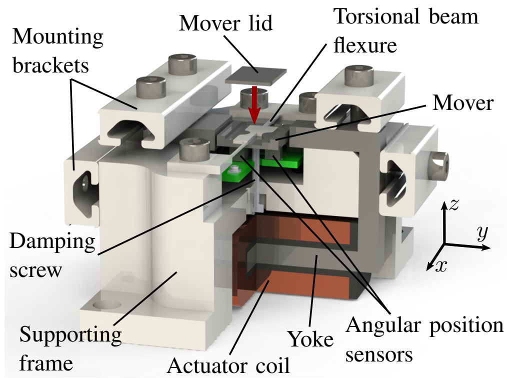

Fig. 5. 1 DoF Scanning system with integrated resonant rotataional reluctance actuator. The mover is connected to the supporting frame via the torsional beam flexure. The ferromagnetic yoke and the actuator coil are connected via mounting brackets. Beneath the mover the angular position system is located.

III. Scanning System Prototype

A. Setup Components

Based on the scanning mirror design from the previous section, a prototype setup is built. The partly assembled system prototype is shown in Fig. 6a. In the front the ferromagnetic yoke is visible, which fits into a recess of the supporting frame and is held in place by the mounting brackets. Due to the pulsed current in the actuator coil and the transient magnetic flux, large eddy-currents would be the consequence if the yoke is made out of solid steel. These eddy-currents could limit the system performance due to a phase loss between the magnetic flux $B(t)$ and the actuator coil current i_{act} [30]. Therefore the yoke is manufactured by stacking together electrically isolated steel sheets with $0.5\,\mathrm{mm}$ thickness, reducing the effective conductivity for the eddy-currents. On top of the mover a mirror is attached. The flux transients also occur in the mover, but for manufacturing reasons, it is made out of a solid steel with a lid (see also Fig. 5).

The integrated angular position sensor system is shown in Fig. 6b. It consists of two optical proximity sensors (TCND5000, Vishay Semiconductors) that measure the distance to the mover plate on either side, enabling the dynamic determination of the mover angle θ with a bandwidth of $20\,\mathrm{kHz}$. Sensor covers on either side ensure a constant light environment at the optical proximity sensors. The sensors work in a differential measurement configuration, strongly reducing the unwanted effect of thermal drift. For the calibration of the sensor system an external optical triangulation sensor (optoNCDT 2300-2, Micro-Epsilon Messtechnik GmbH, GER) is used, measuring the mover deflection from above,

Post-print version of the article: D. Pechgraber, E. Csencsics, and G. Schitter, "Resonant Rotational Reluctance Actuator for Large Range Scanning Mirrors," *IEEE/ASME Transactions on Mechatronics*, 2023. DOI: 10.1109/TMECH.2023.3252940

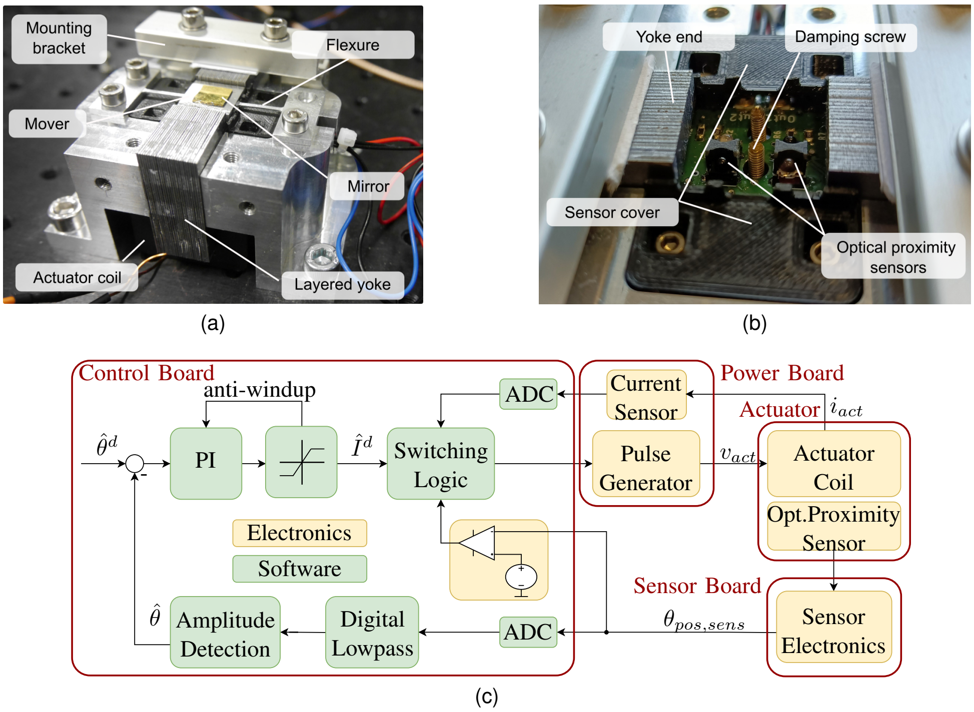

Fig. 6. Experimental prototype system. (a) shows the partly assembled actuator prototype with the layered yoke, which is held in place by the mounting brackets. Further, the mover attached to the torsional beam flexure can be seen with a mirror attached on the top. (b) depicts the details of the angular position sensor system including two optical proximity sensors located below the mover and the damping screw. The sensor covers ensure constant light environment in the viccinity of the optical proximity sensors. (c) shows a block diagram of the entire experimental setup.

revealing a measurement range of $\pm 15\,\mathrm{deg}$ with a resolution of $\approx 25\,\mathrm{m\,deg}$. Further the sharpened damping screw is visible, that is provided for preventing the excitation of the unwanted piston mode of the mover and the flexure.

In Fig. 6c a block diagram of the entire experimental setup is shown (red boxes). The actuator coil is driven by a custom made Power Board which includes a full-bridge pulse generator circuit for driving the coil and a current sensor for measuring the actuator coil current i_{act}. Due to the inductance of the actuator coil of about $7\,\mathrm{mH}$ (see Fig. 3) the driving circuit needs to provide a high voltage output for achieving steep current slopes in the actuator coil. The board can provide an adjustable output voltage of up to $300\,\mathrm{V}$ in the intermediate circuit and includes an Insulated Gate Bipolar Transistor (IGBT) full-bridge circuit for applying either a positive or negative voltage pulse to the actuator coil. For the experiments presented in the paper the voltage pulse is set to $80\,\mathrm{V}$. The pulse generator is controlled by a custom made Control Board, including a 32-Bit microcontroller (Type: STM32F334R8, STMicroelectronics, CHE), on which the control algorithm presented in Section III-C is implemented.

B. Driving Strategy

To uphold an oscillation of the mover, energy has to be injected into the system, in order to compensate the dissipated energy in every oscillation cycle due to material damping. By neglecting the linear and cubic term in (10), the torque applied to the mover can be simplified to

$$\tau(\theta, i_{act}) = -p_2 i_{act}(t)^2 \theta(t) \tag{15}$$

for $i_{act} < 3\,\mathrm{A}$ (see Table II). The negative sign appears, because the torque is directed in the opposite direction of the mover position $\theta(t)$. Assuming a sinusoidal scanning motion of the mover, the torque applied to the mover can then be written as

$$\tau(t, i_{act}) = -p_2 i_{act}(t)^2 \hat{\theta} \sin(\omega_s t) \tag{16}$$

with the scanning amplitude $\hat{\theta}$ and the scanning frequency ω_s. In Fig. 7 these waveforms are shown together with an idealized rectangular shaped actuator current signal. If the current is turned on at $\theta(t) = \hat{\theta}$ and turned off again in the zero-crossing at $\theta(t) = 0$, the energy injected into the system in one actuation cycle can be calculated by

$$\begin{aligned} E_{cycle} = \int \tau(\theta, i_{act}) d\theta &= \int_{\hat{\theta}}^{0} -\left(p_2 \hat{I}^2 \theta(t)\right) d\theta \\ &= \frac{1}{2} p_2 \hat{\theta}^2 \hat{I}^2 , \end{aligned} \tag{17}$$

where $\hat{I}$ denotes the constant current in that time span. It is to note that the integration variable is the mover angle θ in this case, and not the time t. To better understand when, in the time-domain, the energy is injected into the system,

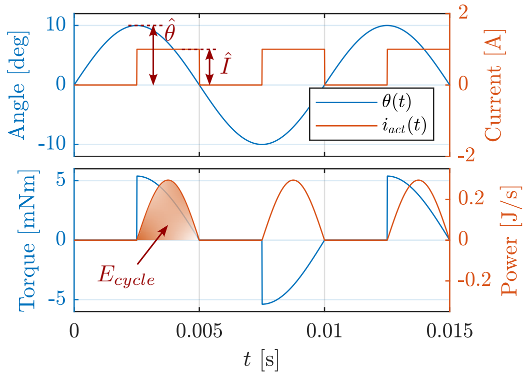

Fig. 7. Idealized actuator current signal $i_{act}(t)$ with mover position $\theta(t)$ result in a torque on the mover, which injects energy into the system. This injected energy can be interpreted as the area below the power curve.

additionally the injected power over time is plotted in Fig. 7. The injected energy per actuation cycle E_{cycle} can then be interpreted as the area below this curve. Although the current slopes can not be infinitely steep in the actuator coil, the simplification made is justified because the contribution to the total injected energy is very low at the beginning and at the end of the current pulse. To now vary the energy injected into the system, and therefore the oscillation amplitude of the mover, either the current amplitude $\hat{I}$, the pulse duration or the relative phase between the oscillation and the current can be changed. The variation of $\hat{I}$ is presented as control strategy in the next section, because in this case the change of energy injected into the system is proportional to $\hat{I}^2$ in every operating point instead of trigonometric functions of t.

C. Controller Design and Implementation

In order to stabilize the oscillation amplitude $\hat{\theta}$, a control strategy is implemented according to Fig. 6c. The amplitude is detected once every oscillation cycle and the current pulse amplitude $\hat{I}$ is varied by a digitally implemented controller. Closed-loop measurements in different operating points $\hat{\theta}$ revealed a first-order low-pass behaviour for the plant $G(s) = \frac{\hat{\theta}(s)}{\hat{I}(s)}$, with corner-frequencies of ≈ 3 Hz. Therefore a tuned PI-controller with the discrete transfer function

$$G_{PI} = \frac{3z - 2.999}{z - 1} \tag{18}$$

and a sampling period of 10 µs is implemented, which leads to an open-loop cross-over frequency of at least 6 Hz and a phase-margin of at least 50 deg in every measured operating point (data not shown). The controller takes the control error between the desired and the detected oscillation amplitude $\hat{\theta}^d - \hat{\theta}$ as input. A switching logic ensures the amplitude of the current peaks and the exact timing of the pulse generator in combination with an external analog comparator circuit, that detects the zero-crossing of the mover position. This approach is similar to the phase locked loop (PLL) control strategy in electro-static driven MEMS mirrors, in which also only pulling forces can be applied to the mover due the electro-static actuation principle [31].

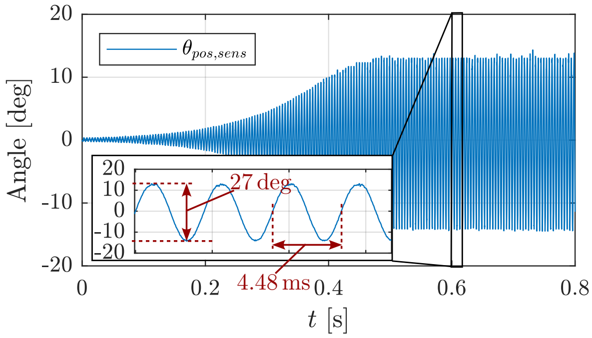

Fig. 8. Swing-up of the mover with feedback control turned off. Current pulses with 50 % duty-cycle, a constant actuation frequency of 446 Hz and a constant amplitude of $\hat{I}^d = 1.2$ A are applied to the actuator coil.

IV. Evaluation of System Performance

The built prototype system is at first evaluated in open-loop configuration, showing the achievable scanning range and scanning frequency. Afterwards the implemented control strategy is evaluated in closed-loop measurements.

A. Open-loop Operation and System Performance

In Fig. 8, the swing-up of the mover to the maximum scanning amplitude $\hat{\theta}$ is shown. Therefore constant current pulses with 50 % duty-cycle and constant actuation frequency of 446 Hz are applied to the actuator coil. The amplitude is slowly increased until at a driving amplitude of $\hat{I} = 1.2$ A the scanning amplitude $\hat{\theta} = 13.5$ deg is attained. Because the theoretical stress limit of the used flexure is nearly reached (see Fig. 4c), the current amplitude is not increased further to avoid damage to the system. Together with the mover aperture size of 15 mm a product of scanning range times mover aperture of 202.5deg · mm is achieved. A scanning frequency of $\frac{1}{4.48\,\text{ms}} = 223$ Hz can be observed, which is slightly lower than expected from the modal analysis in Section II-D. One contributor to this deviation can be found in the additional mass of the mirror attached to the mover. In the frequency spectrum of the position signal a single peak at 223 Hz is visible without any peaks in its vicinity, indicating that the unwanted piston mode is not excited by the actuation (data not shown).

B. Closed-loop Operation

The swing-up of the mover with the implemented feedback control strategy to a desired set amplitude of $\hat{\theta}^d = 4.7$ deg is shown in Fig. 9. With an overshoot of 2 deg the set amplitude is reached in about 100 ms. The jitter of the peak values of $\hat{I}$ and the undershoots below 0 A are due to the sample rate of 10 µs of the microcontroller, which leads to an uncertainty of the switching times.

Due to the solid fabrication of the mover for manufacturing reasons, eddy-current effects are still visible in the current signal of Fig. 9. The delay between the magnetic flux in the circuit and the current i_{act} leads to peaks at the beginning

Post-print version of the article: D. Pechgraber, E. Csencsics, and G. Schitter, "Resonant Rotational Reluctance Actuator for Large Range Scanning Mirrors," *IEEE/ASME Transactions on Mechatronics*, 2023. DOI: 10.1109/TMECH.2023.3252940

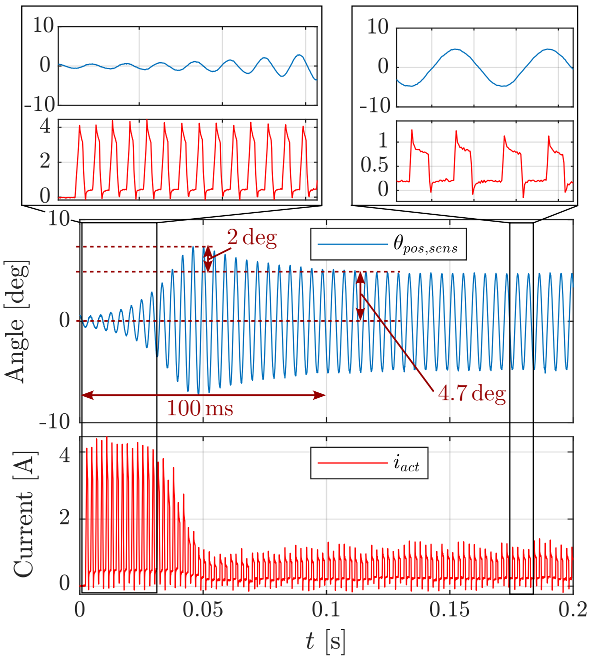

Fig. 9. Swing-up of the mover to a set-amplitude $\hat{\theta}^d = 4.7$ deg with feedback control turned on, reaching the desired set value in ≈ 100 ms. Eddy-current effects in the solid mover are visible in signal shape of the current pulses.

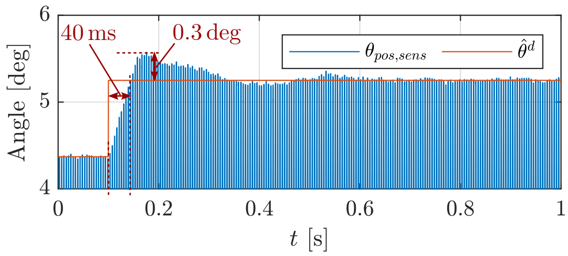

Fig. 10. Step-response from $\hat{\theta}^d = 4.4$ deg to $\hat{\theta}^d = 5.25$ deg.

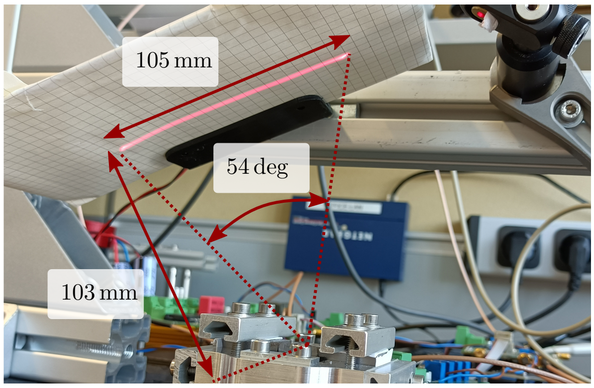

Fig. 11. Scanning of a laser line with feedback control turned off. An optical field of view (FoV) of 54 deg is reached.

and the end of the pulses. Further, it is visible that the switching logic deactivates the full-bridge circuit, when there is still a remaining magnetic flux left in the circuit. Therefore, the measured current jumps back to an offset value after this turn-off transition, and is free-wheeling over the actuator coil's copper resistance. To further reduce the effects of eddy-currents alternative materials with lower electrical conductivity, like silicon-iron or cobalt-iron alloys could be used [32]. The dissipated power of the actuator consists of ohmic losses in the actuator coil and the semiconductor switches, and the core-loss of the magnetic circuit. Due to the full-bridge topology current can be fed back into the supplying intermediate circuit, avoiding any additional power dissipation during the demagnetisation of the coil.

To further investigate the dynamic performance of the implemented control strategy, a step-response from $\hat{\theta}^d = 4.4$ deg to $\hat{\theta}^d = 5.25$ deg is shown in Fig. 10. A rise-time of ≈ 40 ms and an amplitude overshoot of ≈ 0.3 deg can be observed. The overshoot can be explained by dead-time in the system, which is mainly introduced by the amplitude detection only once every oscillation cycle (4.48 ms) and could be reduced with higher phase-margin or smoother reference trajectories.

Figure 11 shows the built actuator in an actual line-scanning setup while driven at the maximum scanning amplitude of $\hat{\theta} = 13.5$ deg. The length of the projected laser line in combination with the distance of the target plane from the mirror reveal an optical FoV of 54 deg, which matches the signals from the integrated optical proximity sensors well.

In summary, the concept of a resonant rotational reluctance actuator is successfully shown, demonstrating a mechanical scanning range of ± 13.5 deg (54 deg optical) and a scanning frequency of 223 Hz with a feedback controlled experimental prototype system.

V. Conclusion

In this paper a 1DoF scanning mirror system based on a novel resonant rotational reluctance actuator is designed, manufactured and evaluated. The novel design, which comprises a large 15 mm mover aperture, places the ferromagnetic yoke on the side of the mover, enabling large scanning ranges compared to the state-of-the-art reluctance actuated systems. The manufactured system prototype achieves a mechanical scanning range of ± 13.5 deg and a scanning frequency of 223 Hz. This clearly meets the set performance goals of ± 12 deg and 200 Hz which results in the performance metric $3.56\text{mm} \cdot \text{rad} \cdot \text{kHz}$ according to [9]. The built prototype system outperforms the state-of-the-art systems in the product of scanning range times mover aperture with $202.5\text{deg} \cdot \text{mm}$, compared to $180\text{deg} \cdot \text{mm}$ [15]. This enables the use in applications with large laser beams in combination with a large optical FoV of 54 deg. Additionally, a control strategy is developed, to allow the driving of the actuator at arbitrary scanning amplitudes.

Future work includes optimization of the scanning mirror system for higher scanning frequencies, advanced flexure design and investigation of additional control strategies to push the control bandwidth further.

Post-print version of the article: D. Pechgraber, E. Csencsics, and G. Schitter, "Resonant Rotational Reluctance Actuator for Large Range Scanning Mirrors," *IEEE/ASME Transactions on Mechatronics*, 2023. DOI: 10.1109/TMECH.2023.3252940

VI. References

[1] H. W. Yoo, M. E. van Royen, W. A. van Cappellen, A. B. Houtsmuller, M. Verhaegen, and G. Schitter, “Automated spherical aberration correction in scanning confocal microscopy,” *Rev. Sci. Instrum.*, vol. 85, no. 12, p. 123 706, 2014.

[2] Q. Zhou, P. Ben-Tzvi, D. Fan, and A. A. Goldenberg, “Design of Fast Steering Mirror systems for precision laser beams steering,” in *ROSE*, 2008, pp. 144–149.

[3] C. Gorecki and S. Bargiel, “MEMS Scanning Mirrors for Optical Coherence Tomography,” *Photonics*, vol. 8, p. 6, 2020.

[4] T. Raj, F. H. Hashim, A. B. Huddin, M. F. Ibrahim, and A. Hussain, “A Survey on LiDAR Scanning Mechanisms,” *Electronics*, vol. 9, no. 5, p. 741, 2020.

[5] J. Huang, Q. Qin, and J. Wang, “A Review of Stereolithography: Processes and Systems,” *Processes*, vol. 8, no. 9, p. 1138, 2020.

[6] R. D. Loor, “Polygon scanner system for ultra short pulsed laser micromachining applications,” *Physics Procedia*, vol. 41, pp. 544–551, 2013.

[7] H. Chaudhary, S. Khatoon, R. Singh, and A. Pandey, “Fast steering mirror for optical fine pointing applications: A review paper applications: A review paper,” in *CIPECH*, IEEE, 2018.

[8] D. Wang, C. Watkins, and H. Xie, “MEMS Mirrors for LiDAR: A Review,” *Micromachines*, vol. 11, no. 5, p. 456, 2020.

[9] T. Ozaki, N. Ohta, and M. Fujiyoshi, “Highly linear and wide nonresonant two-degree-of-freedom piezoelectric laser scanner,” *Sensors*, vol. 22, no. 11, p. 4215, 2022.

[10] F. Senger, J. Albers, U. Hofmann, *et al.*, “A bi-axial vacuum-packaged piezoelectric MEMS mirror for smart headlights,” in *MOEMS and Miniaturized Systems XIX*, vol. 11293, SPIE, 2020, pp. 27–33.

[11] U. Hofmann, J. Janes, and H.-J. Quenzer, “High-Q MEMS Resonators for Laser Beam Scanning Displays,” *Micromachines*, vol. 3, no. 2, pp. 509–528, 2012.

[12] H. Quan, T. Zhang, H. Xu, S. Luo, J. Nie, and X. Zhu, “Photo-curing 3d printing technique and its challenges,” *Bioactive Materials*, vol. 5, no. 1, pp. 110–115, 2020.

[13] E. Csencsics, J. Schlarp, and G. Schitter, “High-Performance Hybrid-Reluctance-Force-Based Tip/Tilt System: Design, Control, and Evaluation,” *IEEE/ASME Trans. Mechatron.*, vol. 23, no. 5, pp. 2494–2502, 2018.

[14] K. G. K. Periyasamy, V. J. Tan, S. He, and N. Kourtzanidis, “External Electromagnet FPCB Micromirror for Large Angle Laser Scanning,” *Micromachines*, vol. 10, no. 10, p. 667, 2019.

[15] B. H. Shin, D. Oh, and S.-Y. Lee, “A Two-Dimensional Laser Scanning Mirror Using Motion-Decoupling Electromagnetic Actuators,” *Sensors*, vol. 13, no. 4, pp. 4146–4156, 2013.

[16] E. Csencsics and G. Schitter, “Exploring the Pareto Fronts of Actuation Technologies for High Performance Mechatronic Systems,” *IEEE/ASME Trans. Mechatron.*, vol. 26, no. 2, pp. 1053–1063, 2021.

[17] F. Li, P. Zhou, T. Wang, J. He, H. Yu, and W. Shen, “A Large-Size MEMS Scanning Mirror for Speckle Reduction Application,” *Micromachines*, vol. 8, no. 5, p. 140, 2017.

[18] B. Cong, J. Schlarp, and G. Schitter, “Iterative learning control for the active error correction of polygon mirror based laser scanning,” in *(AIM)*, IEEE, 2022.

[19] R. M. Schmidt, G. Schitter, and A. Rankers, *The Design of High Performance Mechatronics - 3rd Revised Edition: High-Tech Functionality by Multidisciplinary System Integration*. IOS Press, 2020.

[20] H. W. Yoo, S. Albert, and G. Schitter, “Accurate analytic model of a parametrically driven resonant MEMS mirror with a fourier series-based torque approximation,” *J. Microelectromechanical Syst.*, vol. 29, no. 6, pp. 1431–1442, 2020.

[21] A. Frangi, A. Guerrieri, R. Carminati, and G. Mendicino, “Parametric resonance in electrostatically actuated micromirrors,” *IEEE Trans. Ind. Electron.*, vol. 64, no. 2, pp. 1544–1551, 2017.

[22] A. Champneys, “Dynamics of parametric excitation,” in *Encyclopedia of Complexity and Systems Science*, Springer New York, 2009, pp. 2323–2345.

[23] M. Pumphrey, N. Alatawneh, and M. A. Janaideh, “Modeling and analysis of reluctance motion system with asymmetrical air gaps,” *Review of Scientific Instruments*, vol. 93, no. 7, p. 075 001, 2022.

[24] J. D’Errico. “Polyfitn.” (), [Online]. Available: https://de.mathworks.com / matlabcentral / fileexchange / 34765 - polyfitn (visited on 04/14/2022).

[25] Y. Wang, Y. D. Gokdel, N. Triesault, L. Wang, Y.-Y. Huang, and X. Zhang, “Magnetic-Actuated Stainless Steel Scanner for Two-Photon Hyperspectral Fluorescence Microscope,” *J. Microelectromechanical Syst.*, vol. 23, no. 5, pp. 1208–1218, 2014.

[26] H. Urey, C. Kan, and W. O. Davis, “Vibration mode frequency formulae for micromechanical scanners,” *J. Micromech. Microeng.*, vol. 15, no. 9, pp. 1713–1721, 2005.

[27] C. Zhang, G. Zhang, and Z. You, “A Two-Dimensional Micro Scanner Integrated with a Piezoelectric Actuator and Piezoresistors,” *Sensors*, vol. 9, no. 1, pp. 631–644, 2009.

[28] L. Ye, G. Zhang, and Z. You, “Large-Aperture kHz Operating Frequency Ti-alloy Based Optical Micro Scanning Mirror for LiDAR Application,” *Micromachines*, vol. 8, no. 4, p. 120, 2017.

[29] L. Mouas, H. Mohellebi, and S. H. Ould Ouali, “Experimental study and numerical simulation of magnetization involved in S235 sheets used in the construction of ship hulls,” *Results in Physics*, vol. 14, p. 102 430, 2019.

[30] E. Csencsics, J. Schlarp, and G. Schitter, “Bandwidth extension of hybrid-reluctance-force-based tip/tilt system by reduction of eddy currents,” in *AIM*, 2017, pp. 1167–1172.

[31] D. Brunner, H. W. Yoo, and G. Schitter, “Linear Modeling and Control of Comb-Actuated Resonant MEMS Mirror With Nonlinear Dynamics,” *IEEE Trans. Ind. Electron.*, vol. 68, no. 4, pp. 3315–3323, 2021.

[32] D. Gerada, A. Mebarki, N. L. Brown, C. Gerada, A. Cavagnino, and A. Boglietti, “High-speed electrical machines: Technologies, trends, and developments,” *IEEE Trans. Ind. Electron.*, vol. 61, no. 6, pp. 2946–2959, 2014.

Daniel Pechgraber is doctoral researcher at the Automation and Control Institute (ACIN) at TU Wien, Vienna, Austria. He received an MSc. degree in Electrical Engineering from TU Wien in 2022. His primary research interests are on high performance mechatronic systems design and high precision motion control of linear and non-linear systems.

Ernst Csencsics is assistant professor for Metrology Systems in the Advanced Mechatronic Systems group at the Automation and Control Institute (ACIN) of TUWien. He received an MSc and a PhD degree (sub auspiciis) in Electrical Engineering from TU Vienna, Austria in 2014 and 2017, respectively. His primary research interests are on high performance mechatronic systems, the development of holistic methods for multidisciplinary system design and integration, opto-mechatronic measurement and imaging systems, precision engineering, and robot-based in-line measurement systems. He received the journal best paper award of IEEE/ASME Transactions on Mechatronics (2018) and the best student paper award at the American Control Conference (2016).

Post-print version of the article: D. Pechgraber, E. Csencsics, and G. Schitter, “Resonant Rotational Reluctance Actuator for Large Range Scanning Mirrors,” *IEEE/ASME Transactions on Mechatronics*, 2023. DOI: 10.1109/TMECH.2023.3252940

Georg Schitter is Professor for Advanced Mechatronic Systems at the Automation and Control Institute (ACIN) of TU Wien. He received an MSc in Electrical Engineering from TU Graz, Austria (2000) and an MSc and PhD degree from ETH Zurich, Switzerland (2004). His primary research interests are on high-performance mechatronic systems, particularly for applications in the high-tech industry, scientific instrumentation, and mechatronic imaging systems, such as AFM, scanning laser and LIDAR systems, telescope systems, adaptive optics, and lithography systems for semiconductor industry. He received the journal best paper award of IEEE/ASME Transactions on Mechatronics (2018), of the IFAC Mechatronics (2008-2010), of the Asian Journal of Control (2004-2005), and the 2013 IFAC Mechatronics Young Researcher Award. He served as an Associate Editor for IFAC Mechatronics, Control Engineering Practice, and for the IEEE Transactions on Mechatronics.

Post-print version of the article: D. Pechgraber, E. Csencsics, and G. Schitter, "Resonant Rotational Reluctance Actuator for Large Range Scanning Mirrors," *IEEE/ASME Transactions on Mechatronics*, 2023. DOI: 10.1109/TMECH.2023.3252940